Mapping of Amide, Amine, and Aliphatic Peaks in the CEST Spectra of Murine Xenografts at 7 T

Kimberly L. Desmond,[1] Firas Moosvi,[1,2] and Greg J. Stanisz[1,3]*

Purpose: To evaluate the performance of endogenous chemical exchange saturation transfer (CEST) spectra and derived maps in a longitudinal study of tumor xenografts to ascertain the role of CEST parameters in describing tumor progression and in distinguishing between tumor, muscle, and necrosis.

Methods: CEST spectra of 24 mice with tumor xenografts (20 LLC and 4 MDA) were acquired at three time-points. We employed a novel method of decomposing the CEST spectrum into a sum of four Lorentzian shapes, each with a corresponding measured amplitude, width and frequency offset. This semi-quantitative method is an improvement over techniques which simply assess the asymmetry in the spectrum for the presence of CEST, due to the fact that it is not confounded by CEST peaks on opposing sides of the direct effect. The CEST images were compared to several other commonly employed contrast mechanisms: T_1 relaxation, T_2 relaxation, diffusion (ADC), and magnetization transfer (MT).

Results: Tumor spectra had distinct CEST peaks corresponding to the presence of hydrogen exchange between free water and amide, amine, and aliphatic groups. All three CEST peaks (amide, amine, and aliphatic) were larger in the tumor tissue as compared with the adjacent healthy muscle.

Conclusions: CEST contrast (particularly the amine peak amplitude) performed especially well in distinguishing areas of apoptosis and/or necrosis from actively progressing tumor, as validated by histology. **Magn Reson Med 71:1841–1853, 2014. © 2013 Wiley Periodicals, Inc.**

Key words: CEST; chemical exchange saturation transfer; tumor; Lorentzian; amide; amine; aliphatic

Magnetic resonance imaging has proven successful for the identification of cancer and can provide high-resolution (sub mm) and high-contrast images of the disease. While these capabilities are useful, there is further potential for MRI contrast to represent a specific biomarker and furthermore to obtain quantitative estimates of these biomarkers. Methods such as DCE-MRI (1) and quantitative T_1/T_2 (2,3) are well-established examples, and more recently chemical exchange saturation transfer (CEST) MRI has been applied in the characterization of cancer (4–6). It has been hypothesized that changes in CEST contrast reflect changes in the tumor microenvironment (7). More specifically, altered CEST contrast can represent changes in the local chemical environment of specific metabolites, and has been linked to altered cellular metabolism pathways and apoptosis (8,9). CEST contrast is a means for exploring the changes in tumor metabolism and cellular density associated with tumor growth and response to therapy (10,11). Many CEST studies have focused on a single proton pool of interest, specifically amide proton transfer (APT) (5,12); however, the purpose of this study is to assess the entire CEST spectrum and thereby examine the behavior of the labile protons in tandem for a more complete understanding of the system. Correlates were identified between the CEST-derived contrast and more traditional MRI imaging methods such as T_1 and T_2 mapping, magnetization transfer ratio, apparent diffusion coefficient mapping as well as histology.

CEST contrast is induced by the effects of a saturation pulse applied at the resonance frequency of protons which are in exchange with freely moving water (i.e., with a short correlation time, $\tau_c \sim 10^{-10}$ s) (13). The exchange interaction results in a reduction of signal in the free water, which is detectable as a decrease in intensity of the MRI image. A spectrum can be generated by acquiring an image with CEST-contrast across a range of saturation pulse frequencies, and is known as the CEST-spectrum or Z-spectrum. The amplitude of the CEST spectrum at each offset frequency reflects a steady state between the exchanging proton pools and free water, which is a function of their resonance frequency, relaxation rates, concentration, and the exchange rate constant. It is important to note that the features of the CEST spectrum are not exclusively due to the processes of chemical exchange; there are also contributions from magnetization transfer (from saturation and cross-relaxation of immobile macromolecules) and direct saturation of free water. Lipids, such as triglycerides present in adipose tissue, will be evident in the CEST spectrum as peaks at the methyl and methylene frequencies due to fat saturation effects (14,15). The dominant moeities which contribute to the observed spectra in cancerous tissue are amide groups attached to the backbone of mobile proteins, and amine groups. Mobile lipids and other aliphatics also cause signal decrease via a combination of direct saturation and the Nuclear Overhauser Effect (NOE) (16). Much of the research has focused on the amide proton signal, leading to the definition of the amide proton transfer ratio (APTR) reflecting the relative CEST contrast arising from the amide protons which resonance at ~3.5 ppm. The results have shown an increase in the APTR inside the tumor which is considered to be reflective of the higher protein content (4). Another hypothesis

[1]Department of Medical Biophysics, University of Toronto, Toronto, Canada.

[2]Currently at: University of British Columbia, Vancouver, Canada.

[3]Department of Physical Sciences, Sunnybrook Research Institute, Toronto, Canada.

*Correspondence to: Greg Stanisz, Ph.D., Sunnybrook Research Institute, 2075 Bayview Avenue, S672, Toronto, M4N 3M5, Canada. E-mail: stanisz@sri.utoronto.ca

Received 14 February 2013; revised 18 April 2013; accepted 3 May 2013

DOI 10.1002/mrm.24822

Published online 25 June 2013 in Wiley Online Library (wileyonlinelibrary.com).

is that the increased CEST contrast is related to an increase in the base-catalyzed exchange rate as a result of increased pH within the tumor cells where the majority of the proteins reside (17).

This work examines the methodology for producing an entire CEST spectrum for a single RF power chosen to induce a large amide effect in vivo in a heterotopic tumor model in mice. This results in a CEST spectrum that contains several distinct features, which we attribute to the direct effect, amide, amine, aliphatic groups, and magnetization transfer (MT). We incorporated a fast, semi-quantitative method of describing the CEST spectrum in terms of a sum of Lorentzian shapes in order to produce CEST amplitude maps.

METHODS

A longitudinal study was performed in two heterotopic models of cancer in mice: the invasive murine cell-line Lewis lung carcinoma (LLC) and a human breast cancer cell line (MDA MB-231, hereafter referred to as "MDA") which advances much more slowly and forms a tumor with a large necrotic core. Parametric maps of the dominant features of the CEST spectra were constructed and the progression of the tumors was observed at several time-points. The objective of the study was to determine whether the CEST metrics changed substantially over the course of tumor growth, and whether this was related to the tumor microenvironment as observed in histology.

Animal Model

Twenty-four SHO mice (SCID hairless outbred, Charles River Canada, aged 4–6 weeks) were injected with a 200 μL volume of medium containing up to 2 million tumor cells subcutaneously in the hind limb (20 LLC animals and 4 MDA). For the LLC model, the first imaging session was performed 1 week after the implantation procedure, and for the MDA model imaging was performed 2 months following implantation; in both cases when the tumor had reached a minimum of 0.5 cm in diameter. During imaging sessions, the mice were induced under 5% isoflurane and maintained at 2%; reduced to 1.5% after 1 hour had elapsed. Body temperature was maintained at 37°C by a bath circulating warm water. The animal protocol was approved by the local ARC panel at Sunnybrook Research Institute.

Following the last imaging session, the animals were sacrificed under anaesthetic by cervical dislocation. Tumors were excised, leaving the skin and a layer of muscle below the tumor intact. The excised tissue was then frozen in cryogel. The frozen blocks were cut into five sections spaced 1 mm apart and originating at the largest axial diameter of the tumor (with respect to the imaging orientation). Several 5 μm slices were taken from each section and stained with hemotoxylin and eosin (H&E) for morphological identification and terminal deoxynucleotidyl transferase dUTP nick end labeling (TUNEL) for apoptosis and necrosis.

MRI Imaging

Animals were imaged on a 7 T preclinical MRI (Bruker Biospin) three times: a week post-implantation and for two additional time-points at 2-day intervals from the first scan for LLC and at 2-day and 20-day intervals for MDA. A large volume coil was used for transmission and a Rat Brain (Bruker Biospin) surface coil was used to receive the signal. The CEST imaging sequence consisted of a single rectangular off-resonance RF pulse of 490 ms in duration, followed by a spoiled gradient-echo (FLASH) readout with TR/TE = 500/3.1 ms at a resolution of 0.5 × 0.5 × 2 mm. This sequence was performed with saturation pulse amplitude of 0.57 μT and the off-resonance frequency ranged between −2000 and 2000 Hz (±6.71 ppm) in increments of 50 Hz and with 5 reference images at 200 kHz interspersed throughout the acquisition to allow retrospective correction for signal drift (18). The choice of saturation pulse amplitude was determined from simulations based upon a model (19) which optimized the amide CEST contrast for sensitivity to small changes in amide concentration for expected in vivo conditions.

The magnetization transfer sequence consisted of a train of 12 sinc-shaped pulses for a total duration of 60 ms at RF power of 5.89 μT for frequency offsets of 200, 20, 10, 8, 6, 4, 3, 2, and 1 kHz. T_1-weighted images were acquired with a fast spin-echo inversion recovery sequence (RARE factor of 8), with inversion times (TI) of 0.1, 0.5, 1, 1.5, 2, 3, and 4 s and TR = 10 s. T_2-weighted images were acquired with a standard spin-echo sequence (MSME) with a train of 16 echoes, TE/TR = 11/2500 ms. Diffusion-weighted images were acquired with an EPI readout (4 segments, TE/TR = 25/3000 ms, 2 averages, 6 directions), for b-values of 300 and 500 s/mm^2.

Each of the MT, T_1, T_2, and diffusion-weighted images were acquired for the same FOV and resolution as the CEST spectrum images. Fast spin-echo images (RARE) with 8 echoes per TR were acquired at a resolution of 0.1 × 0.1 × 1 mm with five slices as a reference to aid in definition of ROIs.

The time to acquire the CEST spectrum images was ~60 min. The MT spectra took 10 min, T_1 mapping lasted 9 min, and 5 min each for T_2 and diffusion. The total time to run the protocol for each animal including setup and positioning was ~2 h.

Image Correction

Substantial corrections were required to remove the influence of confounding factors from the data due to inconsistencies in the B_0 field as well as temperature fluctuations. A signal drift was observed which resulted in a reduction in the signal amplitude by several percent over the course of the CEST spectrum acquisition.

In general, the shape of the signal drift over time was consistent. This allowed it to be corrected by fitting a bi-exponential function to the reference images acquired at 200 kHz, normalized to the signal of the first image. This function was extrapolated to each time point during the acquisition of the CEST spectrum, and each image was corrected by dividing by the drift signal at the corresponding time of acquisition. An example of the observed signal drift and the fitted correction curve is shown in Figure 1.

Despite performing a first-order shimming procedure, B_0 fluctuations over the field of view were observed

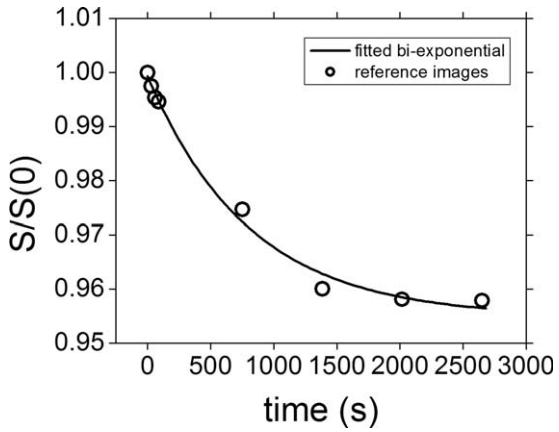

FIG. 1. Signal drift. Signal drift over the course of acquisition of a CEST spectrum. The saturation pulse was 0.6 μT for 490 ms every TR (500 ms) using a rat brain surface coil (Bruker Biospin). An average signal drop of 5% was consistently observed in reference images acquired with a saturation pulse applied at 200 kHz offset frequency.

which ranged from ±500 Hz across the tumor volume. This was due to the location of the tumor at the extremity of the animal causing susceptibility artifacts at the air-tissue interface. To account for this effect, the water peak in the CEST spectra was shifted to 0 Hz offset on a voxel-wise basis. This correction was based upon fitting a single Lorentzian to the data and determining the offset at which the minimum of the direct effect occurred. This is similar to the WASSR B_0 correction (20), with the distinction being that the method used in this work does not use a separate acquisition with higher RF power. A B_0 field map (based on a dual-echo gradient echo sequence) was obtained at the end of the CEST spectrum acquisition to compare with the map obtained from the minimum of the direct effect. These image corrections were performed prior to any ROI averaging operations.

Determination of Metrics

Parametric maps were constructed reflecting the properties of the Z-spectrum peaks by using a peak-fitting algorithm in MATLAB (Peak Fitter for MATLAB, T. O'Haver) which decomposed each CEST spectrum into four Lorentzian lineshapes yielding the amplitude, width, and area of each peak (Eq. [1]), with the residual signal classified as MT effects. This method is a simplified form of the analysis of CEST spectra performed by Zaiss et al. (21).

$$\text{signal}(\Delta) = 1 - \sum_{i=1}^{n} A_i \left(1 + \left(\frac{\Delta - \Delta_{oi}}{0.5^* w_i} \right)^2 \right)^{-1} \quad [1]$$

where $n = 4$, representing the direct effect, amide, amine, and aliphatic peaks in the CEST spectrum as a function of offset frequency (Δ), peak full width at half maximum (w) and amplitude (A). The CEST peak resonance frequency, Δ_0, was fixed at 0, 1050, 600, and −900 Hz for the direct effect, amide, amine, and aliphatic peaks, respectively. This equation provides a phenomenological description of the CEST spectrum, and the approximation breaks down if one enters the regime of coalescence (the exchange rate is too fast, the RF saturation pulse is too strong, or the exchanging pool resonates too close to the water resonance). Of the CEST peaks investigated, the amine peak comes closest to violating the conditions of the approximation; however, we found that for the CEST spectra collected in these experiments there were not large residuals in the amine region of the spectrum, so we concluded that the approximation was sufficient to describe the observed behavior. The peak fitting algorithm operated by inverting the CEST spectrum between −2000 and 2000 Hz and removing the remaining baseline such that the points at −2000 and 2000 Hz corresponded with 0 amplitude. The RF pulse was weak enough for these experiments that the contribution of MT to the spectra was minimal, and after the baseline correction was all but removed entirely. The validity of this procedure is examined further in the Discussion. We differ in this regard to the work of Zaiss who modeled MT effects by an additional Lorentzian shape (21). The decomposition of the CEST signal into Lorentzian peaks is shown in Figure 2. T_1 parametric maps were constructed by fitting the inversion recovery data for each voxel to a model of IR signal as a function of T_1, inversion time and TR (22,23). T_2 parametric maps were calculated by fitting the multi-echo data for each voxel to a single-exponential function. The CESTRasym was also calculated and reflected the degree of asymmetry in the spectrum at 3.5 ppm (∼1050 Hz at 7 T) using the following equation:

$$\text{CESTRasym}(3.5\,\text{ppm}) = \frac{M_z(-1050\,\text{Hz}) - M_z(1050\,\text{hz})}{M_z(200\,\text{kHz})} \quad [2]$$

where M_z refers to the signal intensity as a function of offset frequency . Similarly for MTR, which is a metric describing the amount of magnetization transfer:

$$\frac{\text{MTR} = M_z(200\,\text{kHz}) - \text{Mz}(1.5\,\text{kHz})}{M_z(200\,\text{kHz})} \quad [3]$$

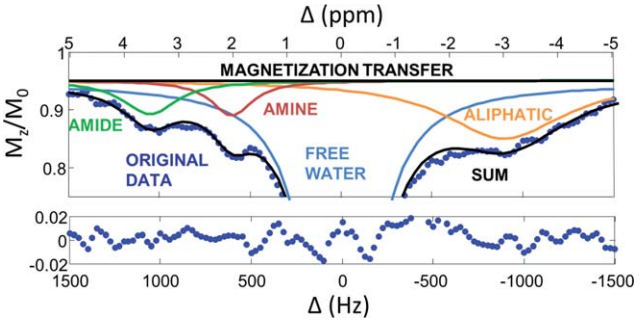

FIG. 2. Peakfit decomposition. Lorentzian decomposition of the CEST spectrum with the peakfit method, with peaks assigned at offset frequencies (Δ) of −900, 0, 600, and 1050 Hz for the aliphatic, free water, amine and amide proton pools, respectively. The amplitude and width of the peaks was allowed to vary in achieving the best fit. Close to the water resonance and for a long, weak RF pulse, the manifestation of magnetization transfer in these spectra is as a broad, essentially featureless, offset from maximum signal. The bottom half of the figure shows the residuals computed between the sum of the fitted peaks and the original data.

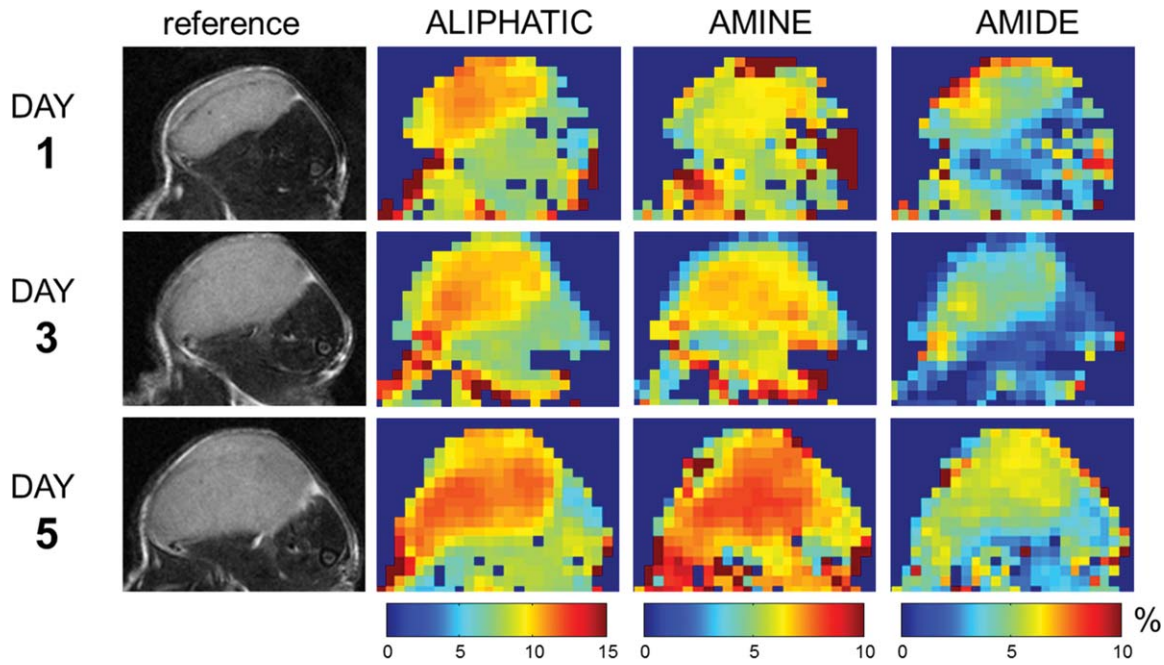

FIG. 3. LLC tumor progression. Maps are shown for the amplitude measurement of the aliphatic, amine, and amide peaks in an LLC xenograft on the hind leg of a single animal followed over a 5-day period, with MRI scans at 2-day increments. Maps were produced from the output of the peak-fitting algorithm, and show the pattern of CEST amplitude increase with tumor progression. Reference images are from a 0.1 × 0.1 × 1 mm^3 slice of a fast spin-echo acquisition.

A tumor size metric was computed by counting the number of tumor voxels in the high resolution fast spin echo data set and converting this to a measurement in mm^3.

The apoptotic index was calculated for each histology slice as the proportion of TUNEL stained area within the slice divided by the total tumor-containing region. Since the vividness of the stain varied between slices, and also due to inconsistencies in the digitization procedure, apoptotic regions on each slide were manually selected and a final filter was calculated from the color values within this region.

ROI Generation

Muscle and tumor masks were automatically generated using an expectation maximization Gaussian mixture model (24) (algorithm obtained from Matlab Central File Exchange, Mathworks) which combined the data from the T_1, T_2, MTR and ADC maps to segment out similar tissue regions. Briefly, the model assumes that the voxels belonging to each tissue type are part of a Gaussian distribution in the four-dimensional parameter map space. The iterative technique assigns each voxel to a cluster such that the log likelihood function (probability that voxel belongs to assigned cluster) is maximized. CEST voxels were excluded from the ROI averages if the result was more than 2 standard deviations from the average or if there was more than 3% residual deviation between the CEST spectrum and the peakfit result (implying poor data quality or a failure in the fitting algorithm), or if the direct effect at 0 Hz offset was less than 87% (implying incomplete saturation due to extreme field inhomogeneity or reduced RF penetration).

RESULTS

The data from one of the LLC animals on the first scan day was discarded due to improper placement of the imaging plane (it did not capture the maximum axial diameter of the tumor). One of the MDA animals prematurely reached the tumor load endpoint of 1.5 cm maximum external diameter and was sacrificed after the first day of scanning.

Signal Drift

Before correction, a signal drop within the tumor ROIs of 7 ± 3% was observed between reference images acquired at the beginning and end of the CEST spectra acquisition (Fig. 1).

CEST Maps and Parameter Progression

An example of the CEST peak amplitude maps (aliphatic, amide, and amine) computed with the peak-fitting algorithm is shown in Figure 3. The properties of the CEST spectra of LLC tumors were found to increase over time (Fig. 3). Figure 4 shows histograms of the CEST amplitude for the LLC animal shown in Figure 3 for each time point, highlighting the trend towards higher amplitude as the tumor grows. The CEST amplitude (average computed over entire tumor ROI) was plotted as a function of tumor size for each experiment in each animal (Fig. 5). This change was correlated with the growth of the tumor (linear r values of 0.51, 0.34,

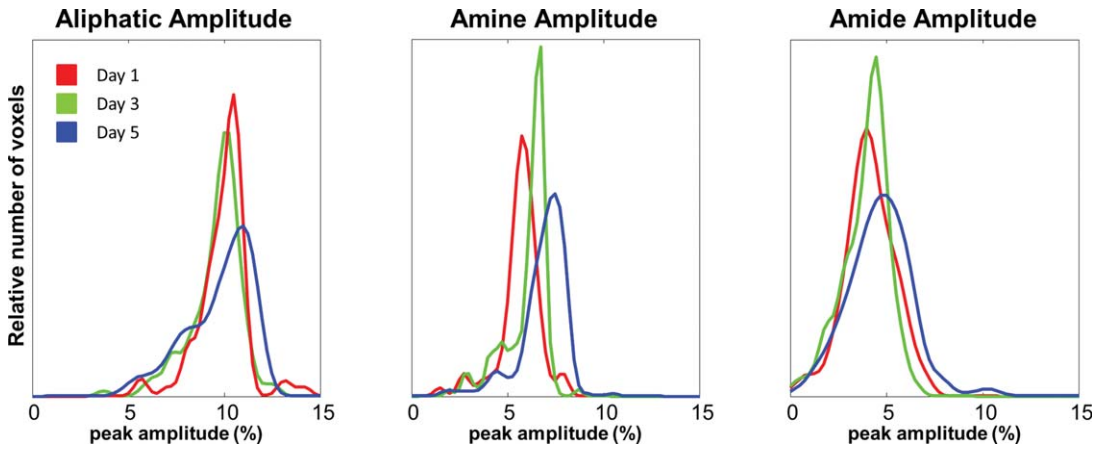

FIG. 4. Histograms for single animal showing progression. Histograms of relative number of voxels in the maps for a single animal for each CEST peak amplitude over the three scan dates (days 1, 3, and 5). There is a progression towards higher amplitude with increasing time as the tumor volume increases.

and 0.17 for aliphatic, amine, and amide peak amplitude vs. tumor size). For a sample size of 52, values of r greater than 0.27 were considered significant ($P < 0.05$). A similar trend was not observed in the MDA data, likely because the MDA tumors were much more heterogeneous. Since the MDA tumors progressed slowly, changes were not expected over a 2-day period and thus these experiments served as an opportunity to assess the reproducibility of the experiment (Fig. 6).

Differences Between Tissue Types

In all maps the tumor had elevated CEST as compared with the nearby muscle tissue. Each parameter map was averaged over the tissue ROI (Fig. 7), for each animal in order to quantitatively evaluate the tissue differences. Although the CEST amplitude slightly increased with tumor volume (Fig. 5), the magnitude of the change was small with respect to the mean parameter value. Therefore, we decided to group the data from all scan days since it did not greatly impair the comparison of CEST parameters between different tissue types (Fig. 7, Table 1) or correlation with other contrast mechanisms. Hypothesis testing with Student's t-test indicated that all tissue types (muscle, tumor, necrosis) had significantly different mean CEST amplitudes ($P < 0.05$). The differences in the mean tumor CEST amplitudes were not significantly different between the LLC and MDA tumor types. The CEST amplitude metrics had the best performance for distinguishing between active tumor and necrotic tissue ($P < 0.01$ for each CEST peak), with MTR the only other metric which could distinguish between the two tissue types with statistical significance ($P < 0.05$). The worst-performing metric was CESTRasym which failed to distinguish between any of the tissue types ($P > 0.2$).

Comparison with Other Contrast Mechanisms

Figure 8 shows a typical dataset in a single animal for LLC, with MRI contrast maps for CEST, MT, T_1, T_2, ADC, and histology. The corresponding dataset for MDA tumors is shown in Figure 9. The correlation coefficients, r, for parameter pairs including tumor volume, aliphatic amplitude, amine amplitude, amide amplitude, T_1, MTR, T_2, CESTRasym, and ADC were computed. Aside from the previously described correlations between tumor volume and the CEST amplitude, several notable correlations (or absences of correlations) were observed (Fig. 10). T_1 was found to be correlated with both the aliphatic and amide peak amplitude ($r = 0.56$ and 0.61, respectively). The aliphatic and amide peak amplitudes were also correlated with each other ($r = 0.72$), whereas the amine and amide peak amplitudes had no correlation ($r = 0.00$). Weak correlations were present between amine and amide if only voxels from muscle were considered.

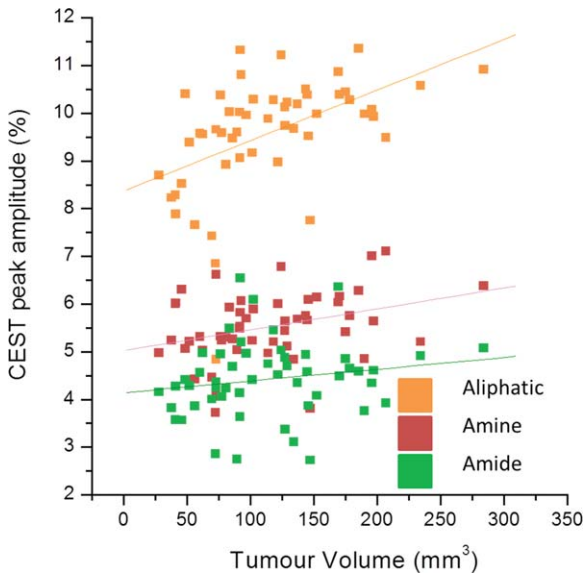

FIG. 5. LLC tumor progression PLOT. CEST peak amplitude as a function of tumor volume. Data is from all LLC animals, for each imaging time-point. Correlation values for the three linear fits are $r = 0.51$, 0.34, and 0.17 for aliphatic, amine and amide respectively, with significance ($P < 0.05$) established at $r = 0.27$.

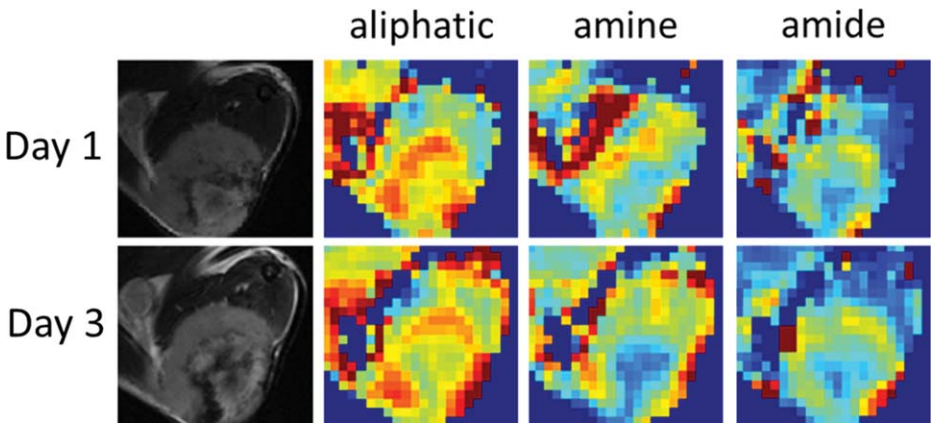

FIG. 6. Reproducibility. A set of CEST amplitude maps showing reproducibility between days 1 and 3 scans of the slow-growing MDA tumor xenograft in the hind leg of a single animal. A necrotic core is clearly visible as a heterogeneous dark-bordered mass in the reference spin echo images, and as reduced peak amplitude in the CEST maps.

DISCUSSION

The CEST metrics allowed for a more specific interpretation of the changes taking place within the tumor microenvironment, since they could be isolated to a single species of exchanging proton. CEST peak amplitude was a more robust alternative to typical asymmetry measures since it was only dependent on the properties of a single peak and thus not impacted by the presence of other CEST species on the contralateral side of the direct effect.

Signal Drift

The signal drift was similar to that observed by Levesque et al. while performing MT and CEST experiments (25). In our case, the source of the signal drift was determined

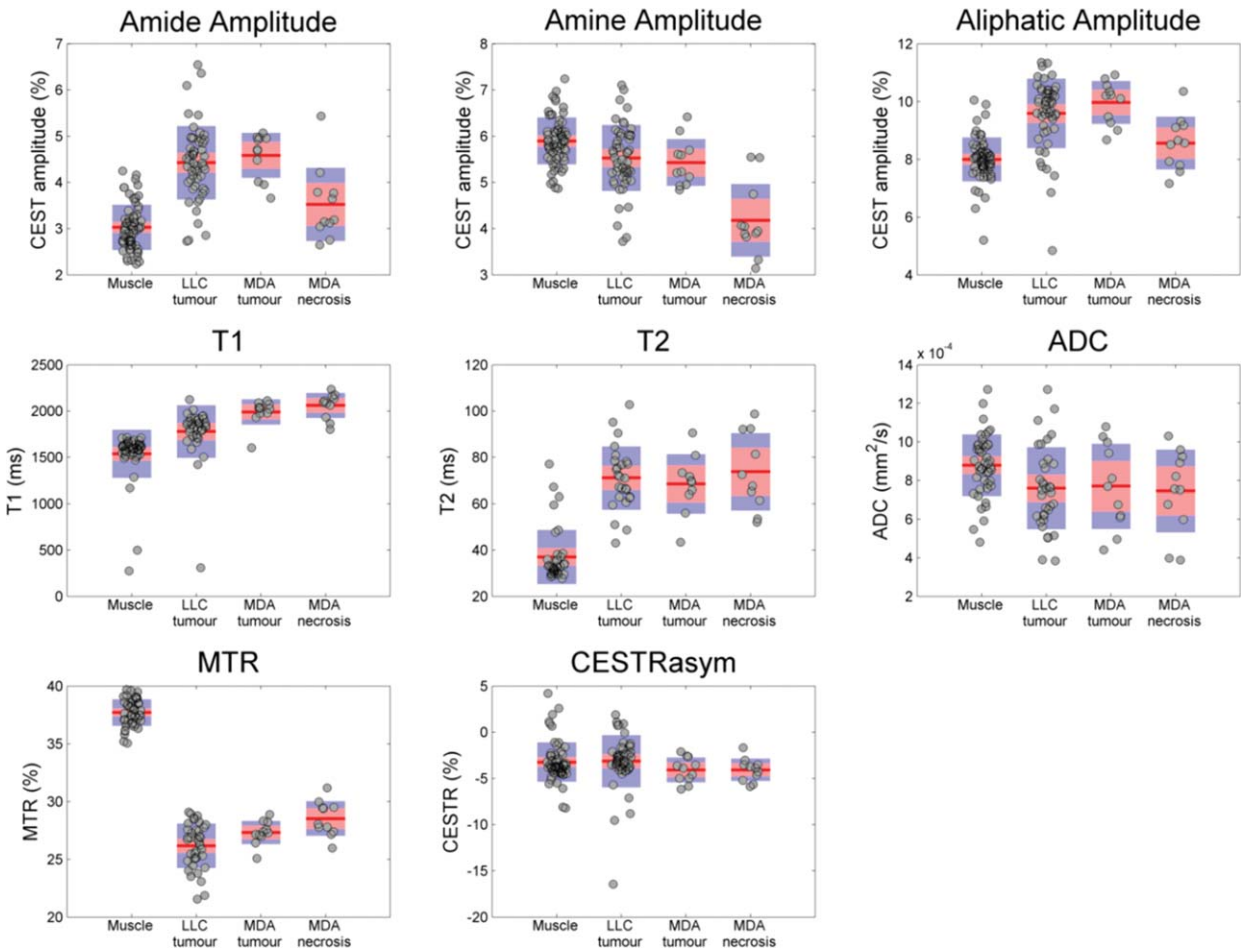

FIG. 7. Bar graphs. ROI averages were computed from the maps from each animal for all scan days (mean ROI values and standard deviation shown in Table 1), and separated into categories based upon tissue type (muscle, LLC tumor, MDA tumor, MDA necrosis). The red line indicates the mean value, the pink shaded region is the 95% confidence interval and the blue shaded region covers one standard deviation from the mean.

Table 1
Metrics ("*n*" Counts Imaging Sessions)

Metric	Muscle ($n = 65$)	LLC (tumor) ($n = 52$)	MDA (tumor) ($n = 11$)	MDA (necrotic) ($n = 11$)
Amide peak amplitude (%)	3.0 ± 0.5	4.4 ± 0.8	4.6 ± 0.5	3.5 ± 0.8
Amine peak amplitude (%)	5.9 ± 0.5	5.5 ± 0.7	5.4 ± 0.5	4.2 ± 0.8
Aliphatic peak amplitude (%)	8.0 ± 0.8	9.6 ± 1.2	10.0 ± 0.8	8.6 ± 0.9
T_{1obs} (ms)	1590 ± 260 ($n = 48$)	1780 ± 290	1990 ± 140	2060 ± 140
T_2 (ms)	40 ± 10 ($n = 36$)	70 ±10 ($n = 26$)	70 ± 10 ($n = 10$)	70 ± 20 ($n = 10$)
ADC (mm^2/s)	$(0.88 \pm 0.16) \times 10^{-3}$ ($n = 46$)	$(0.76 \pm 0.76) \times 10^{-3}$ ($n = 35$)	$(0.77 \pm 0.22) \times 10^{-3}$	$(0.75 \pm 0.21) \times 10^{-3}$
MTR (%)	38 ± 12 ($n = 44$)	26 ± 2 ($n = 38$)	27 ± 1	29 ± 2
APTR (%)	−3.2 ± 2.2 ($n = 63$)	−3.1 ± 2.8 ($n = 51$)	−4.1 ± 1.3	−4.1 ± 1.2
Tumor volume (mm^3)	–	115 ±56	220 ± 115	–

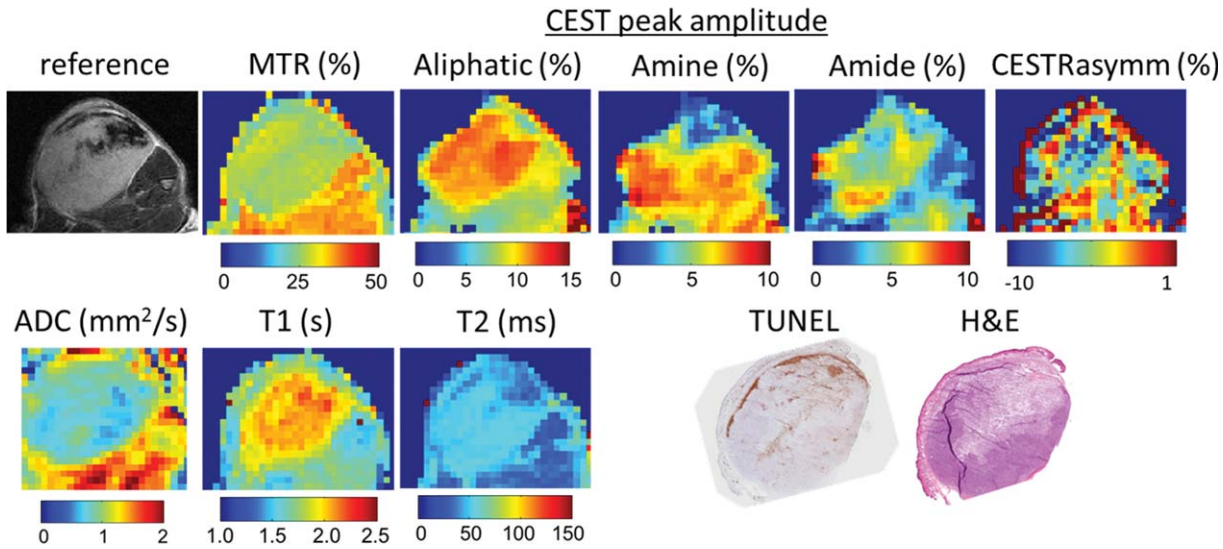

FIG. 8. LLC contrast mechanism comparison. A visual comparison of the maps generated from each MRI contrast mechanism examined in this study, for a single scan time-point in a single LLC animal. Also shown, are the reference spin echo image and the TUNEL and H&E histology images.

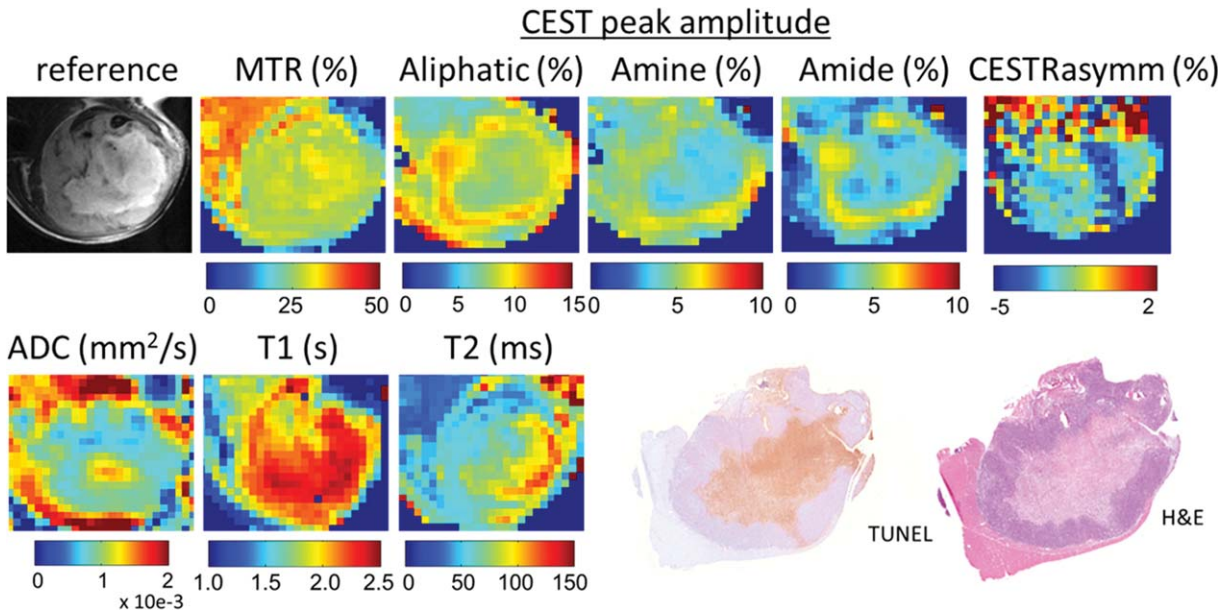

FIG. 9. MDA contrast mechanism comparison. A visual comparison of the maps generated from each MRI contrast mechanism examined in this study, for a single scan time-point in a single MDA animal. Also shown, are the reference spin echo image and the TUNEL and H&E histology images.

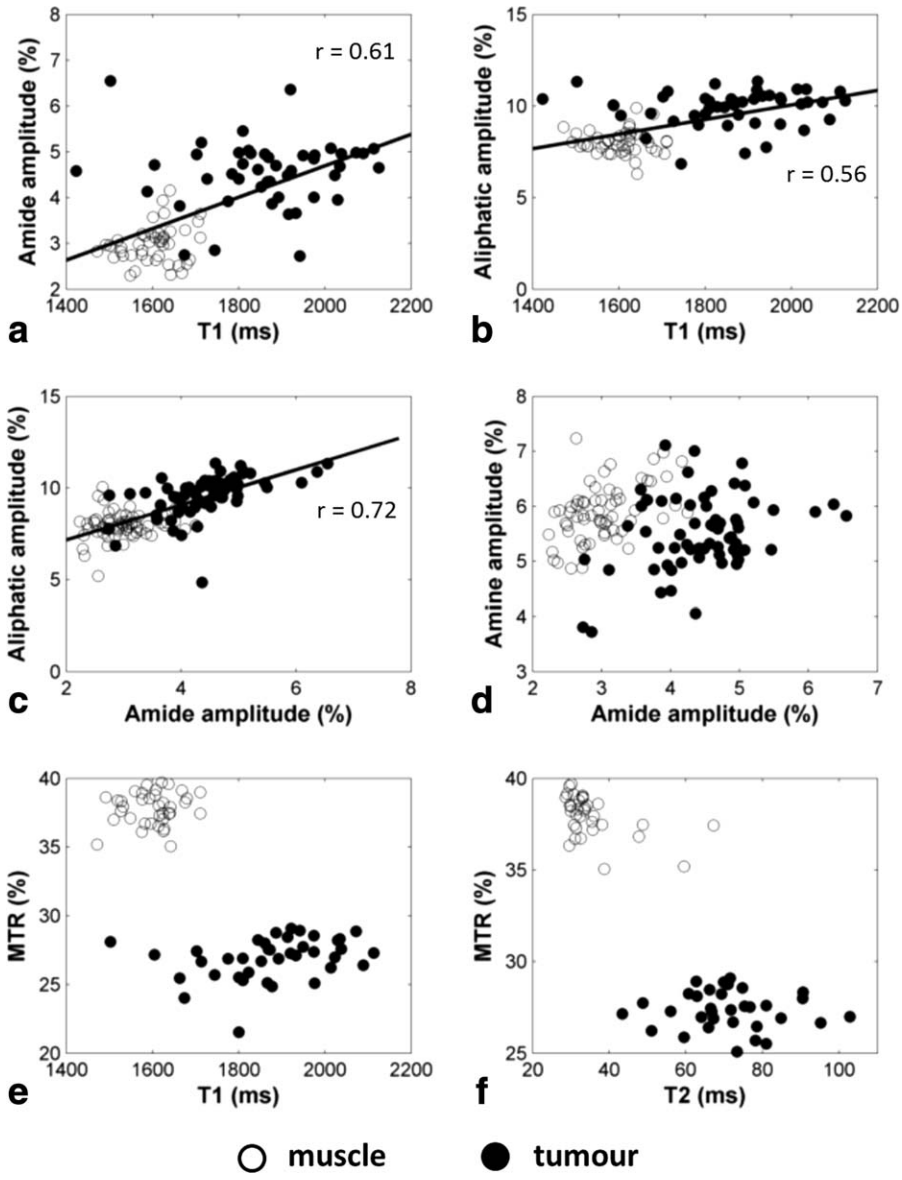

FIG. 10. Parameter correlations. A selection of relevant linear correlations relating the CEST parameters and the other contrast mechanisms. Data are taken from healthy muscle and tumor ROI averages of maps from all LLC and MDA animals on each scan date. Correlation coefficients are shown where a statistically significant relationship was observed. Closed circles represent data from tumor ROIs and open circles represent data from muscle ROIs.

to be heating in the surface coil and preamplifier caused by the high RF duty cycle. In preliminary experiments (data not shown) signal drift was not evident when the experiment was performed with a volume coil, but the surface coil was preferable for subsequent experiments due to the > 3 times increase in SNR. Since the greatest rate of change occurred at the beginning of the experiment, even for short experiments care must be taken to account for this change in signal. This would impact an asymmetry measurement which would differ by several percent depending on the order of image acquisition. Acquiring a set of dummy images prior to the image series may not be practical, since from our observation, the signal took at least half an hour to reach a steady state. Since signal changes were correlated with temperature in the sample and in the coil, instead of acquiring numerous reference images as in this study, a retrospective correction might also be performed by recording the temperature of the coil and of the sample over the course of the exam.

B_0 Correction Method

An accurate B_0 map was crucial for the CEST experiment. Calibration by using a B_0 map acquired prior to the CEST image acquisition was not an ideal solution since in some regions the static field changed by more than 50 Hz within the time during which CEST spectrum was acquired due to temperature variation. As with this study, previous studies have used a single B_0 map to retrospectively correct each image in the spectrum. This is accomplished by various methods including shifting the direct effect of the spectrum to 0 Hz in each voxel (26), acquiring a two-echo B_0 map (27), or with water saturation shift referencing (WASSR) (20). Ideally, one

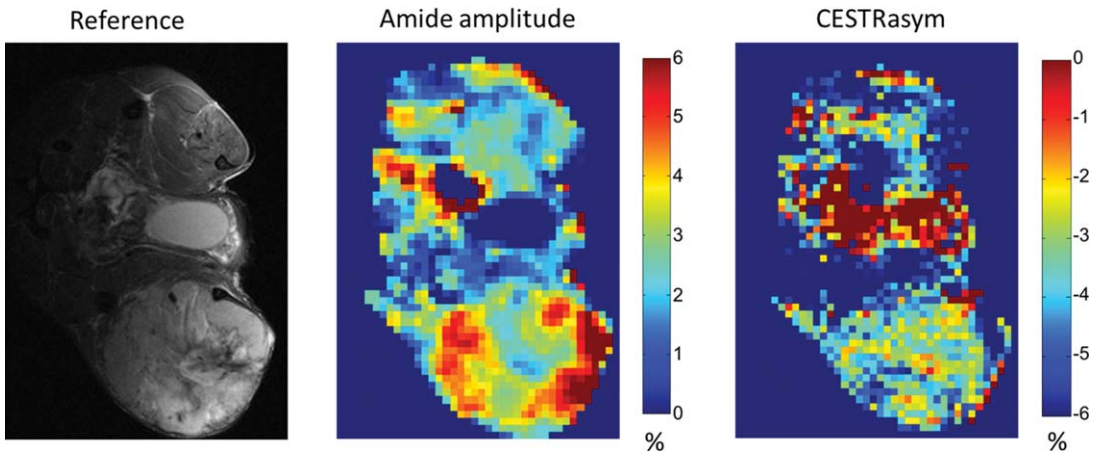

FIG. 11. CESTRasym vs. peakfit. Comparison between the amide peak amplitude and an CESTRasym map. Color bars represent a 6% spread in the map values. The CESTRasym is predominantly negative due to a large contribution from the aliphatic portion of the spectrum on the opposite side of the direct effect from the amide proton resonance.

would have a B_0 map reference for every image of the CEST spectrum (28).

CEST Asymmetry vs. Peakfit

The CESTRasym (computed as in Eq. 1 at 3.5 ppm) technique has evolved from the magnetization transfer ratio (MTR) as a quick means to determine the presence of a saturation transfer effect and its relative magnitude between different tissue types. It is founded on the assumptions that the MT spectrum is symmetric and the CEST spectrum is asymmetric, and also that there are not competing CEST peaks at the same absolute offset frequency. A pH-dependent relationship between the CEST asymmetry and pH has been observed , which led it to be called pH-weighted contrast by some authors (29). In the frequency range of the endogenous CEST spectrum (±10 ppm) and for the RF power used for this experiment (0.57 μT), the asymmetry method becomes less enlightening because of the location of the aliphatic and amide CEST effects at approximately −900 and 1050 Hz, respectively. We observed large differences between CEST in three tissue groups: muscle, tumor, and necrosis, which were much less evident when using the CESTRasym (Fig. 11). This may appear contradictory to other studies in cancer which found a positive CESTRasymm of several percent at 3.5 ppm (4,5,30–32); however, there is evidence showing a negative CESTRasymm in benign prostate cancer (32) and in studies at field strengths greater than 3 T (31). Although different tumor models were used in this study, it is expected that CESTRasym maps would be similarly poor regardless of tumor type, since LLC and MDA represent a substantially different subset of tumor types. It is suspected that the cause for the differences in CESTRasymm contrast is the fact that the prior studies were performed at 3 T rather than 7 T as done in this work. The aliphatic effect is not prominent in the 3 T data, and has less of an influence on the CESTRasymm. These studies also tended to use a stronger RF pulse for saturation (1–3 μT) which would have increased the contrast in the asymmetry maps. as opposed to the 0.6 μT used in this work. For this study, since the magnitude of the aliphatic effect is generally larger than that of the amide effect, the CESTRasym is negative and any pH estimates based upon it would be more strongly influenced by the aliphatic concentration, which conflicts with its intended use as a metric describing the amide pool.

Effect of MT on the Peakfit Results

Since all the proton pools (bulk water, CEST and MT) are directly or indirectly connected and exchanging magnetization, the signal observed in the saturation transfer experiment is a nonlinear function of the properties of each involved pool (19). For this reason it is imprecise to assume that the CEST spectrum is an addition of discrete Lorentzian-shaped contributions from each pool; however, it is the simplest approach given the desire to create parameter maps with limited computer processing time.

Given that MT was best able to distinguish tumor from muscle amongst all the contrast mechanisms examined (Fig. 7), it may seem counterintuitive to neglect its contribution to the CEST spectrum except as a constant offset in the data. One must bear in mind, however, that the maximum contrast in the MT spectrum occurs beyond several thousand Hz offset frequency, which is well beyond the reach of the CEST spectrum at 7 T and that the lower RF power used for CEST experiments is not as effective at generating MT contrast (19). The effects of MT asymmetry, estimated to be on the order of 1.5% at maximum for this experiment (data not shown), were also not directly accounted for in the peakfit model, however, as long as this feature is broad and slowly varying it should not have a significant impact on the determination of the CEST peak amplitudes. Through simulation (detailed in Ref. (19)), we briefly explored the validity of the assumptions made in the peakfit algorithm as compared with a fully determined quantitative three-pool model. Unless otherwise stated, the parameters used in the simulated data were: CEST proton

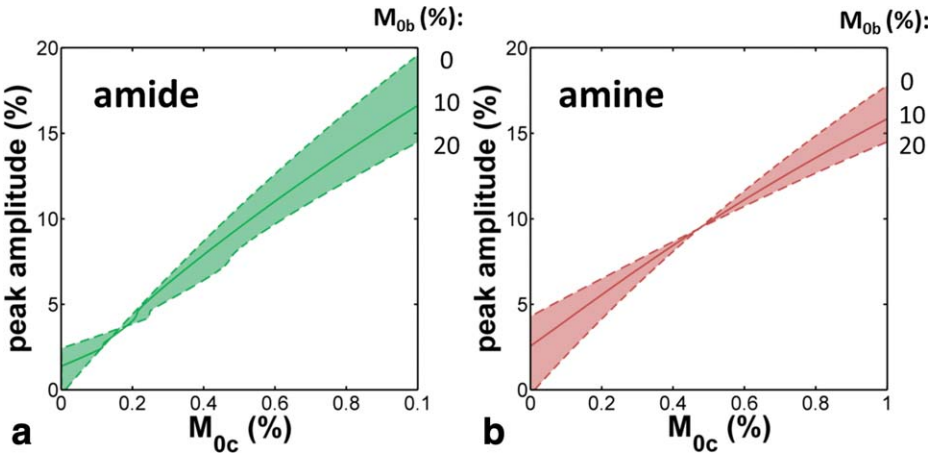

FIG. 12. Peakfit assumptions. Simulation relating the CEST pool fraction (M_{0c}) to the peak amine and amide amplitude from the Lorentzian decomposition of the signal, showing the influence of the macromolecular pool fraction (M_{0b}) upon the output of the peakfit algorithm. Three cases are shown for each CEST pool; M_{0b} = 0, 10, and 20% representing the whole physiological range of M_{0b}.

fraction (M_{0c}) = 0.0015, MT proton fraction (M_{0b}) = 0.1, observed $1/T_1$ ($R1_{obs}$) = 0.5 s^{-1}, T_2 of bulk water pool (T_{2a}) = 70 ms, T_2 of MT pool (T_{2b}) = 10 μs, T_2 of CEST pool (T_{2c}) = 20 ms, exchange constant for CEST pool (R_{CEST}) = 20 s^{-1} (amide), 1000 s^{-1} (amine), exchange constant for MT pool (R_{MT}) = 40 s^{-1}, frequency shift of CEST pool (Δ_{0c}) = 1050 Hz (amide), 600 Hz (amine), $1/T_1$ of MT pool (R_b) = 1 s^{-1}, $1/T_1$ of CEST pool (R_c) = 1 s^{-1} and the sequence parameters as stated above in the Methods section.

We considered the relationship between the peak amplitude and M_{0c}, the CEST fraction relative to bulk water, under the effects of different sized MT pools (Fig. 12). Changing M_{0b} by ± 10% results in less than 5% deviation in the peak amplitude. This simulation is over-cautious because M_{0b} is not expected to change substantially in cancerous tissues regardless of apoptotic status (33). M_{0c} for the amide pool has been estimated to be ~0.15% (17) with the amine M_{0c} expected to be similar in magnitude since the size of both pools is correlated with protein concentration, at which point the amide peak amplitude appears to be invariant with M_{0b}. For high M_{0c} and M_{0b}, the peak amplitude is underestimated because, since the CEST and MT pools are in equilibrium, the CEST peak height is reduced by M_{0b} (19,34). In the limit of very low M_{0c}, the peakfit algorithm overestimates the peak height by incorrectly assigning some of the spectral features, which are actually due to MT, to the CEST peak. It should be cautioned that the peakfit method is only semi-quantitative and cannot be used to determine M_{0c} without first adjusting for the MT contribution determined by a proper quantitative fit of the MT parameters (35).

Alternative Line Shapes

The motivation for the decomposition of the spectrum into four fixed-position Lorentzian-shaped peaks was due to the fact we were aware of four features (two dominant CEST pools, the aliphatic pool, and the direct effect) that in the limit of slow exchange and with sufficient peak separation would be Lorentzian (21,36). Fixing the offset frequency of the peak does affect the results, although it takes deviations of 100 Hz or more from the optimal value to affect the peak amplitude by 1%. Furthermore, the extent of the error in the peak amplitude is related to the width of the peak, such that the amplitude of the aliphatic peak is less affected by these types of errors.

The reduced χ^2 values for the single-voxel fit were computed as follows:

$$\text{reduced}\,\chi^2 = \frac{1}{N - np - 1}\sum\frac{(O-E)^2}{\sigma^2} \qquad [4]$$

where N is the number of frequency offsets sampled, np is the number of free parameters in the fit, O is the observed signal, E is the model fit, and σ is the standard deviation of the observed signal. A reduced χ^2 of 1 is ideal, less than 1 implies overfitting, and greater than 1 implies that the model does not contain sufficient free parameters to describe the data. For the four-Lorentzian, single voxel fit with fixed offset frequency the reduced χ^2 values were close to (but less than) 1, and thus adding any further complexity to the model was not warranted. This situation changed when the spectra were averaged over an ROI, reducing the noise by a factor of 10–20 depending upon the number of ROI voxels and increasing the reduced χ^2 substantially. Further complexity in the fit was introduced by allowing the offset frequency to become a free parameter, which is logical because the apparent offset frequency of the pools would change depending on the proton exchange rate. This decreased the value of the reduced χ^2, but it was still much greater than 1. This prompted a search for a more appropriate decomposition function. It was found that if the number of allowed Lorentzian peaks was increased to 5 when fitting the averaged Z-spectrum, then an additional peak emerged at approximately −600 Hz (−2 ppm). This region corresponds with the frequency offset of H-α protons in proteins (37), which can participate in intramolecular NOE with the nearby amide groups so an additional peak may be justified. Another promising method was to introduce parameters for kurtosis and skew by using a Pearson IV lineshape (38), which has the ability to compensate for the asymmetry in the peaks which occurs as the exchange rate increases and the peaks begin to coalesce.

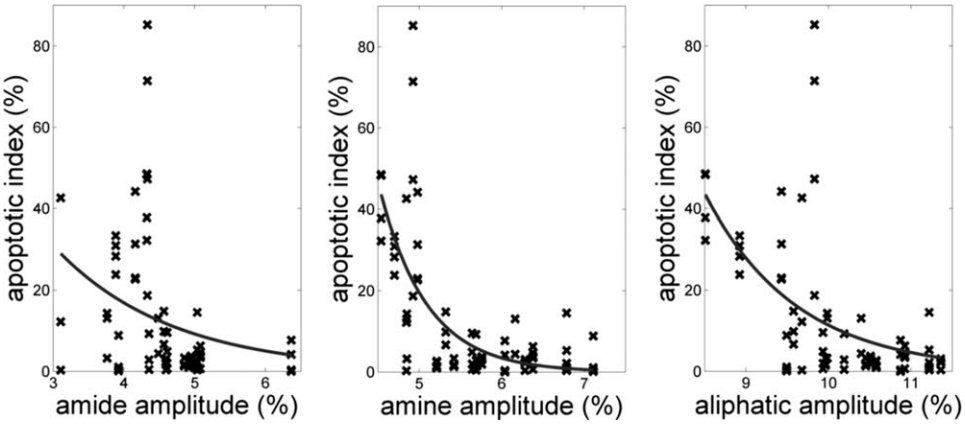

FIG. 13. Apoptotic index. The apoptotic index (area fraction of apoptotic cells within the tumor as determined from TUNEL staining) plotted against the CEST amplitude of the amide, amine and aliphatic peaks. An exponential fit was performed ($y = ae^{bx}$) and r values were 0.53, 0.83, and 0.73 for the amide, amine, and aliphatic curves.

Physiological Source of CEST Effect

Three CEST pools were consistently observed, at −3.0 ppm, 2.0 ppm, and 3.5 ppm in the tumor ROIs. The pool at 3.5 ppm is best characterized in the literature, and corresponds to a base-catalyzed chemical exchange between the backbone amide groups of mobile proteins and peptides and bulk water. Work by Takahashi (39) demonstrated an increased CESTRasymm at 2 ppm in lung cancers and attributed this to amino acid side chain amine groups, while Jin (40) focused on creatine as an additional source. At −3.5 ppm, there is more than one hypothesis for the physiological origin of the feature in the CEST spectrum. It is known that chemical exchange between -CH groups and water is extremely slow, and unlikely to contribute to the CEST spectrum through this mechanism. Direct excitation of lipid groups is one possibility (since the bandwidth of the excitation pulse is broad), and some lipids have been found to be at higher concentration in tumor tissue than in adjacent muscle (41,42). However, fat suppressed experiments do not completely remove the effect at −3.5ppm, suggesting a different mechanism. Another hypothesis is that there are aliphatic groups in the proteins which are strongly coupled with the labile amide groups such that applying a saturation pulse at this frequency will cause the water peak to reduce in amplitude through aliphatic to amide to water magnetization transfer (16,43). In this case the effect at -3.0 ppm would be correlated with the effect at 3.5 ppm. The third, and the generally accepted, mechanism is cross relaxation from dipolar coupling with the bulk water causing a negative (due to the relatively large size of the molecules involved) intermolecular Nuclear Overhauser effect (NOE) (44).

The regions of dark signal on the high resolution spin echo images indicate regions of apoptosis and/or necrosis (as seen in the reference images in Figs. 6 and 8), which are confirmed by the brown staining on the TUNEL histology. CEST parameters are also sensitive to the changing tissue structure with cell death, as the parameters in these regions trend towards what is observed in healthy muscle. Notable is the large reduction of the amine amplitude in necrotic tissue to levels below that of healthy muscle (Table 1), which for this study was the CEST metric most discriminating of apoptotic/necrotic tissue.

Comparison MDA to LLC

The main difference between the two tumor cell lines was the rate of growth with the LLC line behaving much more aggressively. The approximate doubling time for the LLC tumors in this study was 3 days compared with 14 days for the MDA. This is understandable given that the LLC cells are murine in origin whereas the MDA are human. Another distinguishing feature of the MDA tumors was the presence of a large apoptotic/necrotic core. Smaller regions of apoptosis were visible on the histology for the LLC tumors, characteristically at the periphery of the tumor or between tumor lobes. As previously observed (11), CEST performs well in separating necrotic tissue from actively proliferating tumor. The LLC tumors also had a higher propensity for ulceration than the MDA upon exceeding 1 cm in diameter.

It is important to note that the CEST parameters were not static in time for the tumor tissue, and appeared to slightly increase over time (Figs. 3 and 5) as well as have changing histogram features with the tumor growth (Fig. 5). This could have implications for future longitudinal studies, i.e., those assessing the impact of therapy, because, in the absence of proper controls, it may be difficult to establish a baseline and changes due to successful therapy could be masked by changes due to tumor growth.

Parameter Differences Between Tissue Types and Correlations

The amplitude of the CEST peaks was dependent upon T_1, since a longer T_1 ensures that the survival time of the saturation in the bulk water pool is increased. A correlation between the amide and aliphatic amplitude was related to the fact that every amino acid contains an aliphatic and amide group. This diminishes the effectiveness of the CESTasym computation, if CEST amplitudes at both positive and negative offsets are changing similarly then their difference may not change, supported by the noisiness of the CESTRasym maps in Figures 8, 9, and 11.

When tissue types are combined, there is no correlation between the amine CEST and the other CEST peaks. However, when peak amplitudes are separated into tumor and muscle subtypes, there are significant, but still

relatively weak, correlations between amine and amide in muscle. Within the tumor amine and amide remain not significantly correlated. Having a correlation in one tissue type but not another implies that there is a different distribution of exchange rates for either amine or amide protons for each type. Amide protons are most likely not responsible because the amide CEST is dominated by amides on the protein backbone and not likely to have vast differences in structure between muscle and tumor. In the case of amines, it is known that there is a difference in the concentration of creatine between muscle and tumor and thus the muscle amine peak would have a larger contribution from creatine. The amplitude of the amine peak in muscle tissue from this study is significantly ($P < 0.01$) greater than that of the tumor, suggesting that there is an additional non-protein source of amine proton exchange. It is still not readily apparent why this would result in a higher correlation between amine and amide CEST in muscle. We can speculate that the distribution of exchange rates from amine side chains has a much larger standard deviation than that of exchange rates in creatine, and additionally that the muscle tissue has a more consistent intracellular pH which would also reduce the standard deviation of the distribution of exchange rates. Coupling this theory with the fact that the concentration of creatine and protein are likely correlated since they are both related to the amount of muscle tissue, it is probable that the correlation between amine and amide CEST would be stronger in muscle.

The amine amplitude was related to the apoptotic index through an exponential relationship, with an r of 0.83 (Fig. 13). This could be further improved with better colocalization between histology slices and MR images, since for the purposes of this study the apoptotic index from all histology slices was used.

We examined the distribution of the ROI average values of healthy muscle, tumor from the LLC and MDA models, and necrosis (Fig. 7) and the performance of the metrics for distinguishing between the tissue types. It was clear that MTR was most reliably ($P << 0.001$) able to separate the tumors from healthy muscle, a result which echoes previous findings comparing MRI contrast mechanisms in tumors (45,46). The evaluation of tumor heterogeneity, i.e., in discerning necrotic tissue from active tumor, was best accomplished by the CEST amplitude metrics ($P < 0.01$), with the greatest confidence in the amine amplitude ($P < 0.0005$). A previous study by Wen et al., (6) similarly found that CEST metrics (in this case, APT) were able to make this distinction.

CONCLUSIONS

CEST spectra were produced at several time points for LLC and MDA tumors implanted in mice, with care to remove potential confounds from B_0 variations and temperature-related signal drift. The peak-fitting method is robust and allows for fast determination of CEST metrics without requiring multi-pool modelling of the Bloch equations. Results (Fig. 8, in particular) revealed that (for the experimental scanner parameters used in this study), out of all CEST metrics, the aliphatic, and amide CEST properties are best for distinguishing between tumor and healthy muscle tissue, while amine CEST offers the best overall characterization of necrosis. The amide and aliphatic CEST are correlated, suggesting that amide protons could play a role in the aliphatic contribution to the CEST spectrum.

ACKNOWLEDGMENTS

The authors acknowledge funding from the Ontario Institute of Cancer Research and the Canadian Institute of Health Research. They are grateful to Melissa Yin for tumor implantation and Joydeep Chaudhuri for preparation of specimens for histology and for useful discussions.

REFERENCES

1. Tofts P. Modeling tracer kinetics in dynamic Gd-DTPA MR imaging. J Magn Reson Imaging 1997;7:91.
2. MacFall JR, Wehrli FW, Breger RK, Johnson GA. Methodology for the measurement and analysis of relaxation times in proton imaging. Magn Reson Imaging 1987;5:209-220.
3. Poon CS, Henkelman RM. Practical T2 quantitation for clinical applications. J Magn Reson Imaging 1992;2:541-553.
4. Zhou J, Lal B, Wilson DA, Laterra J, van Zijl P. Amide proton transfer (APT) contrast for imaging of brain tumors. Magn Reson Med 2003;50:1120-1126.
5. Jones CK, Schlosser MJ, van Zijl PC, Pomper MG, Golay X, Zhou J. Amide proton transfer imaging of human brain tumors at 3T. Magn Reson Med 2006;56:585-592.
6. Wen Z, Hu S, Huang F, Wang X, Guo L, Quan X, Wang S, Zhou J. MR imaging of high-grade brain tumors using endogenous protein and peptide-based contrast. Neuroimage 2010;51:616-622.
7. Bell LK, Ainsworth NL, Lee SH, Griffiths JR. MRI & MRS assessment of the role of the tumor microenvironment in response to therapy. NMR Biomed 2011;24:612-635.
8. Gillies RJ, Raghunand N, Karczmar GS, Bhujwalla ZM. MRI of the tumor microenvironment. J Magn Reson Imaging 2002;16:430-450.
9. Zhang X, Lin Y, Gillies RJ. Tumor pH and its measurement. J Nucl Med 2010;51:1167-1170.
10. Glunde K, Jacobs M, Pathak A, Artemov D, Bhujwalla Z. Molecular and functional imaging of breast cancer. NMR Biomed 2009;22:92-103.
11. Zhou J, Tryggestad E, Wen Z, Lal B, Zhou T, Grossman R, Wang S, Yan K, Fu DX, Ford E. Differentiation between glioma and radiation necrosis using molecular magnetic resonance imaging of endogenous proteins and peptides. Nat Med 2010;17:130-134.
12. van Zijl P, Jones CK, Ren J, Malloy CR, Sherry AD. MRI detection of glycogen in vivo by using chemical exchange saturation transfer imaging (glycoCEST). Proc Natl Acad Sci USA 2007;104:4359.
13. Wolff SD, Balaban RS. NMR imaging of labile proton exchange. J Magn Reson 1990;86:164-169.
14. Desmond K, Stanisz G. Comparison of tissues characterized by CEST spectra at 7 T. In Proceedings of the 20th Annual Meeting of ISMRM, Melbourne, Australia, 2012. p. 3372.
15. Keller PJ, Hunter W, Schmalbrock P. Multisection fat-water imaging with chemical shift selective presaturation. Radiology 1987;164:539-541.
16. van Zijl P, Zhou J, Mori N, Payen JF, Wilson D, Mori S. Mechanism of magnetization transfer during on resonance water saturation. A new approach to detect mobile proteins, peptides, and lipids. Magn Reson Med 2003;49:440-449.
17. Zhou J, Payen JF, Wilson DA, Traystman RJ, van Zijl PC. Using the amide proton signals of intracellular proteins and peptides to detect pH effects in MRI. Nat Med 2003;9:1085-1090.
18. Desmond K, Stanisz G. pH mapping based on the ratiometric amide and amine relationship from endogenous CEST. In Proceedings of the 3rd International Workshop on Chemical Exchange Saturation Transfer Imaging, Annapolis, Maryland, USA, 2012. p. 30.
19. Desmond KL, Stanisz GJ. Understanding quantitative pulsed CEST in the presence of MT. Magn Reson Med 2012;67:979-990.
20. Kim M, Gillen J, Landman BA, Zhou J, Van Zijl P. Water saturation shift referencing (WASSR) for chemical exchange saturation transfer (CEST) experiments. Magn Reson Med 2009;61:1441-1450.

21. Zaiss M, Schmitt B, Bachert P. Quantitative separation of CEST effect from magnetization transfer and spillover effects by Lorentzian-line-fit analysis of z-spectra. J Magn Reson 2011;211:149-155.
22. Drain L. A direct method of measuring nuclear spin-lattice relaxation times. Proc Phys Soc A 1949;62:301-306.
23. Hahn EL. An accurate nuclear magnetic resonance method for measuring spin-lattice relaxation times. Phys Rev 1949;76:145.
24. Hartley H. Maximum likelihood estimation from incomplete data. Biometrics 1958:174-194.
25. Levesque IR, Stikov N, Pike GB, Pauly JM. Drift in the magnetization transfer signal: effect on quantitative MT experiments. In Proceedings of the 19th Annual Meeting of ISMRM, Montreal, Canada, 2011. p. 2782.
26. Stancanello J, Terreno E, Castelli DD, Cabella C, Uggeri F, Aime S. Development and validation of a smoothing splines based correction method for improving the analysis of CEST MR images. Contrast Media Mol Imaging 2008;3:136-149.
27. Wei W, Jia G, Sammet S, Wassenaar P, Zhou J, Knopp M. Improving amide proton transfer imaging with dual echo B 0 mapping for field inhomogeneity correction at 3T. In Proceedings of the 18th Annual Meeting of ISMRM, Stockholm, Sweden, 2010. p. 2986.
28. Keupp J, Eggers H. CEST-Dixon MRI for Sensitive and Accurate Measurement of Amide Proton Transfer in Humans at 3T. In Proceedings of the 18th Annual Meeting of ISMRM, Stockholm, Sweden, 2010. p. 338.
29. Sun PZ, Zhou J, Sun W, Huang J, van Zijl PC. Detection of the ischemic penumbra using pH-weighted MRI. J Cereb Blood Flow Metab 2007;27:1129-1136.
30. Salhotra A, Lal B, Laterra J, Sun PZ, van Zijl PCM, Zhou J. Amide proton transfer imaging of 9L gliosarcoma and human glioblastoma xenografts. NMR Biomed 2008;21:5.
31. Cai K, Xu HN, Singh A, Haris M, Reddy R, Li LZ. Characterizing Prostate Tumor Mouse Xenografts with CEST and MT-MRI and Redox Scanning. Oxygen Transport to Tissue XXXIV: Springer 2012:39-45.
32. Jia G, Abaza R, Williams JD, Zynger DL, Zhou J, Shah ZK, Patel M, Sammet S, Wei L, Bahnson RR. Amide proton transfer MR imaging of prostate cancer: a preliminary study. J Magn Reson Imaging 2011;33:647-654.
33. Bailey C, Desmond KL, Czarnota GJ, Stanisz GJ. Quantitative magnetization transfer studies of apoptotic cell death. Magn Reson Med 2011;66:264-269.
34. Li AX, Hudson RH, Barrett JW, Jones CK, Pasternak SH, Bartha R. Four-pool modeling of proton exchange processes in biological systems in the presence of MRI-paramagnetic chemical exchange saturation transfer (PARACEST) agents. Magn Reson Med 2008;60:1197-1206.
35. Henkelman RM, Huang X, Xiang QS, Stanisz GJ, Swanson SD, Bronskill MJ. Quantitative interpretation of magnetization transfer. Magn Reson Med 1993;29:759-766.
36. Zhou J, van Zijl PCM. Chemical exchange saturation transfer imaging and spectroscopy. Prog Nucl Magn Reson Spectrosc 2006;48(2-3):109-136.
37. Kowalsky A. Nuclear magnetic resonance studies of proteins. J Biol Chem 1962;237:1807-1819.
38. Pearson K. Contributions to the mathematical theory of evolution. II. Skew variation in homogeneous material. Philos Transact A Math Phys Eng Sci 1895;186:343-414.
39. Takahashi M, Togao O, Kessinger CW, Huang G, Dimitrov I, Sherry AD, Gao J. Characterization of lung cancer by amide proton transfer (APT) imaging: in-vivo study in an orthotopic mouse model. In Proceedings of the 19th Annual Meeting of ISMRM, Montreal, Canada, 2011. p. 3163.
40. Jin T, Wang P, Zong X, Kim SG. Magnetic resonance imaging of the Amine-Proton EXchange (APEX) dependent contrast. Neuroimage 2011;59:1218-1227.
41. Block RE, Maxwell GP, Prudhomme DL, Hudson JL. Brief communication: high resolution proton magnetic resonance spectral characteristics of water, lipid, and protein signals from three mouse cell populations. J Natl Cancer Inst 1977;58:151-156.
42. Kuesel AC, Sutherland GR, Halliday W, Smith ICP. 1H MRS of high grade astrocytomas: mobile lipid accumulation in necrotic tissue. NMR Biomed 2005;7:149-155.
43. Liepinsh E, Otting G. Proton exchange rates from amino acid side chains—implications for image contrast. Magn Reson Med 1996; 35:30-42.
44. Jin T, Wang P, Zong X, Kim SG. MR imaging of the amide-proton transfer effect and the pH-insensitive nuclear overhauser effect at 9.4 T. Magn Reson Med 2013;69:760–770.
45. Lemaire L, Franconi F, Saint-André J, Roullin VG, Jallet P, Le Jeune JJ. High-field quantitative transverse relaxation time, magnetization transfer and apparent water diffusion in experimental rat brain tumor. NMR Biomed 2000;13:116-123.
46. Pui MH, Wang Y. Diffusion and magnetization transfer MRI of brain infarct, infection, and tumor in children. Clin Imaging 2005;29:162-171.